

EHands: Quantum Protocol for Polynomial Computation on Real-Valued Encoded States

Jan Balewski,¹ Chris Pestano,² Mercy G. Amankwah,³ E. Wes Bethel,² Talita Perciano,^{4,*} and Roel Van Beeumen^{5,*}

¹*National Energy Research Scientific Computing Center,
Lawrence Berkeley National Laboratory, Berkeley, CA 94720, USA*

²*Computer Science Department, San Francisco State University, San Francisco, CA 94132, USA*

³*Department of Mathematics, Applied Mathematics and Statistics,
Case Western Reserve University, Cleveland, OH 44106, USA*

⁴*Scientific Data Division, Lawrence Berkeley National Laboratory, Berkeley, CA 94720, USA*

⁵*Applied Mathematics and Computational Research Division,
Lawrence Berkeley National Laboratory, Berkeley, CA 94720, USA*

(Dated: October 7, 2025)

We present **EHands**, a *quantum-native protocol* for implementing multivariable polynomial transformations on quantum processors. The protocol introduces four fundamental, reversible operators—*multiplication, addition, negation, and parity flip*—and employs the Expectation Value ENcoding (EVEN) scheme to represent real numbers as quantum states. Unlike discretization or binary encoding methods, **EHands** operates directly on vectorized real-valued inputs prepared in the initial state and applies a shallow quantum circuit that depends only on the polynomial coefficients. The result is obtained from the expectation value measured on a single qubit, enabling efficient parallel evaluation of a polynomial across multiple data points using a single circuit. We introduce both a *reversible* implementation for degree- d polynomials, requiring $3d$ qubits, and a *non-reversible* variant that uses qubit resets to reduce the requirements to $d + 1$ qubits. Both implementations exhibit linear depth scaling in d and are explicitly decomposed into one- and two-qubit gates for direct execution on current quantum processing units. The protocol’s effectiveness is demonstrated through experimental validation on IBM’s Heron-class quantum processors, showing reliable polynomial approximations of functions like ReLU and arctan.

I. INTRODUCTION

Quantum computing promises to accelerate computation across a wide range of scientific disciplines, with significant breakthroughs such as Shor’s factoring algorithm [1], Grover’s search method [2], and the HHL algorithm for solving linear systems [3]. While problems like quantum dynamics simulation [4] naturally map to quantum hardware, classical computers remain superior for arithmetic operations. Efficient quantum implementations of addition, multiplication, and polynomial evaluation are crucial for enabling end-to-end quantum workflows. It allows avoiding repeated measurement, costly classical post-processing, and quantum state reinitializations, that hinder hybrid approaches.

Polynomial transformations play a key role in interpolation, approximation, and modeling of non-linear functions across science and engineering. Yet current quantum algorithms for such transformations remain limited: they often mimic classical algorithms based on discretization or rely on binary encoding [5–9], leading to deep circuits or large ancilla overhead, impractical for near-term devices. Alternative methods such as quantum signal processing (QSP) [10, 11], quantum singular value transformation (QSVT) [12], and quantum eigenvalue transformation (QET) [13] enable implicit polynomial trans-

formations of singular values or eigenvalues, but are not designed for direct polynomial evaluation on input data prepared in initial quantum states.

Quantum algorithms also differ widely in their sampling requirements. Grover’s algorithm and quantum phase estimation (QPE) are nearly deterministic, requiring only tens of repetitions [14, 15], whereas algorithms like quantum approximate optimization algorithm (QAOA), quantum Monte Carlo, and boson sampling demand thousands to millions of shots to yield reasonable accuracy [16–18]. The protocol introduced here, **EHands**, falls into the latter category: it encodes results in expectation values and thus requires sampling, but achieves this through shallow, structured circuits.

Hybrid variational methods [19] can approximate functions via parameter optimization but require extensive classical-quantum feedback, which is resource-intensive and noise-sensitive. In contrast, **EHands** provides a direct, deterministic quantum-native approach to polynomial evaluation.

This paper makes four main contributions. First, we introduce **EHands**, a protocol that implements a universal set of basic arithmetic operations directly on QPUs using shallow, reversible circuits. Building on these primitives, **EHands** enables multivariable polynomial transformations on data encoded via the Expectation Value ENcoding (EVEN) scheme. Second, **EHands** naturally operates on vectorized inputs, allowing efficient parallel polynomial evaluation across multiple data points in a single quantum circuit. Third, we present both *reversible*

* Corresponding authors: tperciano@lbl.gov, rvanbeeumen@lbl.gov

and *non-reversible* implementations for degree- d polynomials. The reversible version requires $3d$ qubits, while the non-reversible variant leverages resets to reduce the qubit requirement to $d+1$. Both implementations achieve linear depth scaling in d and are explicitly decomposed in one- and two-qubit gates for direct execution on current QPUs. Four, we demonstrate the practicality of **EHands** through experiments on contemporary NISQ hardware, showing reliable accuracy for polynomial approximations of common nonlinear functions.

II. EXPECTATION-VALUE ENCODING (EVEN) SCHEME

To encode a list of $N \geq 1$ real values $x_i \in [-1, 1]$, we construct a product state $|\phi\rangle$ with N qubits, each initialized to the $|0\rangle$ state and subjected to an $R_y(\theta_i)$ rotation, where $\theta_i = \arccos(x_i)$.

To retrieve data from a specific qubit in the EVEN state $|\phi\rangle$, we apply *decoding* by measuring the expectation value (EV) of the Pauli-Z operator for that qubit, given by $\hat{x} = \langle \phi | O | \phi \rangle$. [Figure 1a](#) shows the encoding and decoding of an EVEN state for a single real input x . See [Section A 1](#) for encoding and decoding of 2 real numbers on 2 qubits.

The EVEN is a type of angle encoding [20]. Rather than using a simple linear transformation to convert a real number into a rotation angle within the range $[0, \pi]$, EVEN applies a non-linear transformation via the arccos function. This seemingly minor modification plays a crucial role in simplifying the polynomial transformation protocol described below.

III. THE EHANDS PROTOCOL

We introduce four fundamental reversible quantum operations: (1) *product-with-memory*, (2) *weighted sum*, (3) *negation*, and (4) *parity flip*. [Figures 1b](#) to [1e](#) present their corresponding quantum circuits. These operations will serve as the building blocks for polynomial calculations.

The **product-with-memory** operation is defined by the unitary $U_{\text{prod}} = \text{CNOT}_{0,1} \cdot [I \otimes R_z(\pi/2)]$. [Figure 1b](#) shows its implementation. For the pair of inputs x_0, x_1 , the information about their product is stored in qubit q_1 , while qubit q_0 retains the value of x_0 . The value of x_0x_1 can be retrieved by measuring the EV of the operator $O_p = I \otimes \sigma_z$. Alternatively, additional quantum operations can be applied to either qubit for further computations.

The **weighted sum** operation is defined by $U_{\text{sum}}(w) = [R_y(-\alpha/2) \otimes I] \cdot \text{CNOT}_{1,0} \cdot [R_y(\alpha/2) \otimes I] \cdot U_{\text{prod}}$, shown in [Fig. 1c](#). The parameter $\alpha = \arccos(1 - 2w)$ depends on the chosen relative weight $w \in [0, 1]$, making $U_{\text{sum}}(w)$ a parametric unitary operator. It computes the weighted sum $S_w(x_0, x_1) = wx_0 + (1-w)x_1$, with the result stored

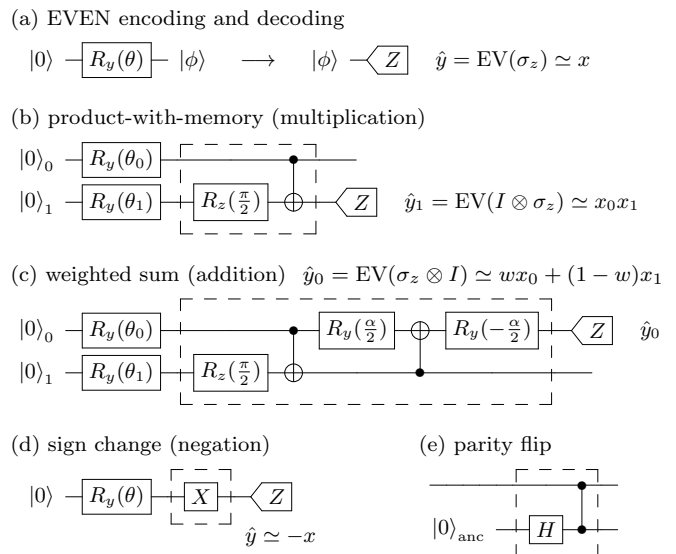


FIG. 1. (a) EVEN encoding of the real number x into the quantum state $|\phi\rangle$ using $\theta = \arccos(x)$, along with its decoding, where the expectation value of the Pauli-Z operator is the estimator \hat{x} . The four building blocks of the **EHands protocol** are represented as circuits: (b) multiplication, (c) addition, (d) negation, and (e) parity flip.

in qubit q_0 . The value of $S_w(x_0, x_1)$ can be retrieved by measuring the EV of the complementary operator $O_s = \sigma_z \otimes I$. Again, further arithmetic operations can be performed on the data encoded in qubit q_0 . Strictly speaking, the weighted sum circuit could also be used for multiplication since q_1 encodes the product x_0x_1 . However, in practice, we prefer the dedicated multiplication circuit shown in [Fig. 1b](#), which requires only 1 CNOT gate. Although qubit q_1 in [Fig. 1c](#) is no longer used it must be preserved for reversibility.

The **negation** operation is implemented using the standard X-gate, as shown in [Fig. 1d](#). Transforming quantum state $x \rightarrow -x$ is particularly useful for overcoming the constraint that the weight w of the $S_w(x_0, x_1)$ operation must be positive. By applying negation to one of the inputs, such as on qubit q_1 in [Fig. 1c](#), the result becomes a weighted difference $S_w(x_0, -x_1) = wx_0 - (1-w)x_1$.

Finally, **parity flip** operation, implemented by the circuit shown in [Fig. 1e](#), is required when multiple addition operations are performed sequentially, e.g., in constructing a polynomial in [Fig. 2a](#). The weighted sum operations can introduce phase factors that manifest as imaginary components in intermediate calculations. The parity flip operation uses an ancilla qubit in superposition to apply controlled-Z gates that cancel these unwanted phase contributions, ensuring the final result remains real-valued as required for polynomial evaluation.

We refer to [Section A](#) for unitary representations and proofs of the correctness of arithmetic and concatenation operations for those circuits.

IV. POLYNOMIAL CONSTRUCTION

Based on the four arithmetic quantum operations of **EHands**, we present a constructive method for computing a degree- d polynomial, $P_d(x)$, on a quantum state. The polynomial is given by:

$$P_d(x) = \frac{1}{d+1} (a_0 + a_1x + a_2x^2 + \dots + a_dx^d), \quad (1)$$

where the input x , the polynomial coefficients a_i , and the output are all real values constrained to the range $[-1, 1]$.

The d copies of the real-valued input x are encoded in an **EVEN** quantum product state on d qubits. To compute $P_d(x)$, we construct a quantum algorithm that sequentially applies addition and multiplication operations, similar to how a polynomial is evaluated on a classical calculator. There are multiple valid approaches to achieve this construction. Our reference implementation proceeds as follows: (i) compute all powers of the input x , (ii) multiply each power x^k by its corresponding coefficient a_k , and (iii) sum the terms sequentially. Since we employ the *dyadic* operation $S_w(a, b)$, which combines only two inputs at a time, a sequence of d such operations is needed to obtain $P_d(x)$.

A complete reversible quantum circuit for computing a degree $d = 4$ polynomial on a real number x is illustrated in [Fig. 2a](#). Due to the *no-cloning* theorem, which prohibits reusing quantum states in multiple operations, four separate copies of the input are required. Since the multiplication operator does not alter the upper qubit, the information stored there can be reused twice, as shown in [Eq. \(A8\)](#) of [Section A](#). The 5 user-defined polynomial coefficients stored in qubits a_i are likewise encoded in an **EVEN** quantum product state. To ensure proper cancellation of unwanted quantum state components, 3 parity flip operations must be applied between successive sum operators. This requires 3 ancilla qubits prepared in superposition, which act as a fair-coin random generators through the applications of CZ gates.

[Fig. 2b](#) shows the non-reversible version of the same $P_4(x)$. The quantum resources required for the reversible and non-reversible implementations of a polynomial $P_d(x)$ are presented in [Table I](#). [Section E](#) showcases yet another implementation of $P_d(x)$ requiring only $\mathcal{O}(\log d)$ depth of CNOT gates.

TABLE I. Resources and connectivity needed for reversible and non-reversible implementations of a polynomial $P_d(x)$. Both implementations require one final qubit measurement.

type	qubits	ancilla	resets	CNOTs	connectivity
reversible	$3d$	$d - 1$	0	$5d - 2$	limited
non-reversible	$d + 1$	0	$2d - 1$	$5d - 2$	linear

A priori, it is not obvious which of the two versions—reversible or non-reversible—will provide higher-fidelity execution on NISQ-era hardware. There is a

trade-off between the noise introduced by the resets versus using a larger number of qubits, some of which may experience long idle times. Also a more demanding connectivity may require additional SWAP operations. Only the reversible **EHands** can be used as an *oracle* for Grover-type search algorithms. However, one can simulate much higher-degree polynomials using the non-reversible version, since classical simulation memory requirements scale exponentially with qubit count.

V. QUANTUM EXPERIMENTS

To validate the **EHands** protocol on real quantum hardware, we selected the three functions listed in [Table II](#) and executed the corresponding **EHands** circuits on IBM’s *Aachen*, *Kingston*, and *Marrakesh*.

Each target function was approximated by a polynomial of the desired degree. During classical pre-processing, the function was tabulated, fitted with a degree- d polynomial, and the resulting coefficients were rescaled so that their maximum absolute value did not exceed 1. The resulting polynomials were then encoded using the **EHands** protocol.

TABLE II. Polynomial approximations of functions computed on real IBM quantum hardware.

target function	Fig. 3 panel	poly degree	num CNOTs ^a	num qubits	used shots ^b
ReLU($x/2$)	a	3	28	9	2e4
arctan($5x$)	b	3	28	9	9e4
$x^2/3$	c	2	14	6	9e4

^a circuit transpiled for heavy-hex qubit connectivity

^b number of shots per x -data point

The results, shown in [Fig. 3](#), demonstrate good agreement with the target functions. To mitigate hardware errors, we employed randomized compilation [21] and optimized qubit mapping [22], while omitting dynamical decoupling and zero noise extrapolation. [Section D](#) contains additional experimental results with each method toggled on and off, and provides a detailed justification for our decisions. The additional simulations for different polynomials are included in [Section C](#). The remaining discrepancies between the results from different QPUs reflect the individual biases introduced by each NISQ device.

VI. DISCUSSION

The **EHands** protocol offers a versatile framework for implementing polynomial computations on QPUs, especially on NISQ devices. By leveraging standard quantum gates, our protocol implements efficient multivariable

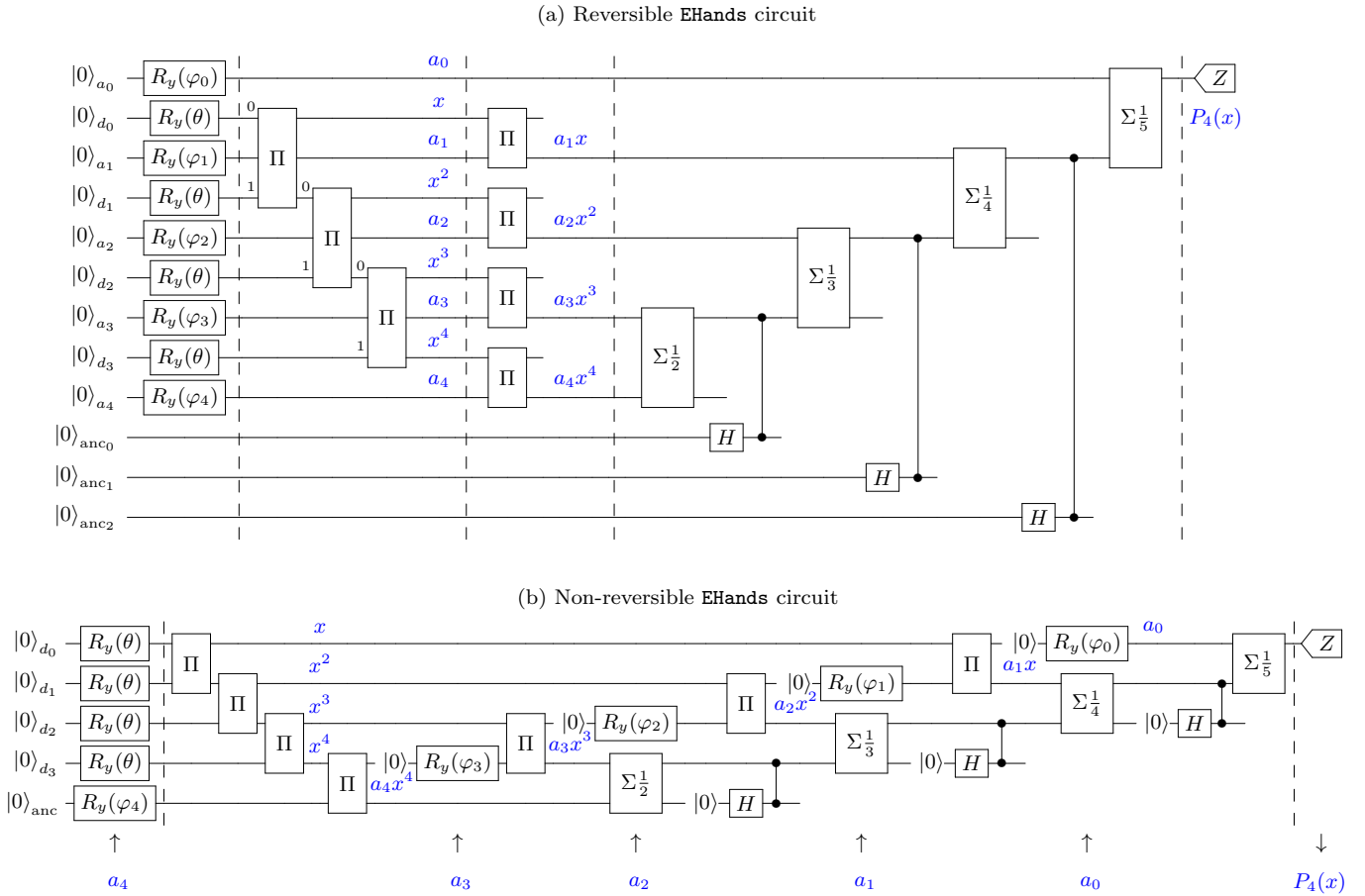


FIG. 2. EHands circuits for a degree-4 polynomial $P_4(x) = \frac{1}{5}(a_0 + a_1x + a_2x^2 + a_3x^3 + a_4x^4)$: (a) *Reversible* 12-qubits EHands circuit for computing $P_4(x)$, where the 4 copies of the input x are stored in qubits d_i , and the 5 polynomial coefficients are encoded in qubits a_i . The 3 ancilla qubits anc_i are needed for concatenation of the 4 sum operators. Note that only qubit a_0 is measured. Unitaries labeled as Π and Σ_w represent the multiplication and addition circuits shown in Figs. 1b and 1c, respectively. (b) *Non-reversible* 5-qubits EHands circuit for the same degree-4 polynomial using only 1 ancilla qubit and many resets allowing for qubit recycling.

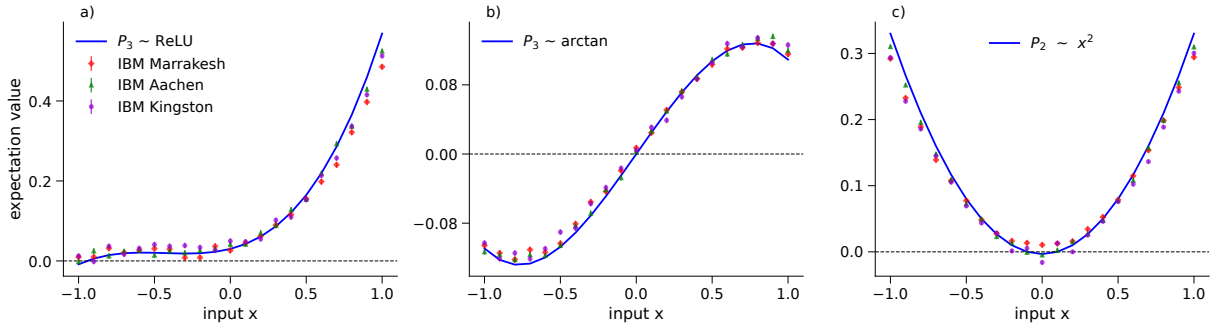


FIG. 3. Hardware results from IBM's *Aachen*, *Kingston*, and *Marrakesh* for polynomial approximations of the functions listed in Table II, where we enabled Pauli twirling to mitigate hardware errors.

polynomial approximations for data stored in the EVEN-encoded initial state. In comparison to the quantum singular value transformation (QSVT) method, which implements polynomial transformations of the singular values of a block-encoded matrix, EHands computes the

polynomial directly on the input data and does not require interleaving the signal operator containing the input data with unitary operators. By directly operating on real-valued data encoded in quantum states, EHands is well-suited for applications with naturally available real-

number inputs, such as sensor data or machine learning features. Experimental results on current quantum hardware demonstrate solid accuracy of the **EHands protocol** when standard error mitigation techniques are applied. As hardware performance improves, we anticipate that even deeper circuits for higher-degree polynomials will yield reliable results.

A key advantage of the **EHands protocol** is its capability to perform *vectorized* polynomial operations. Due to space constraints, this aspect is not explored in detail here. However, by incorporating advanced data encoding schemes such as **QPIXL** [23] and **QCrank** [24], a series of n real-valued data points can be efficiently stored on a QPU using only $\lceil \log_2 n \rceil$ additional address qubits. This integration enables *parallel computation* of the desired polynomial across entire sequences of real numbers, making **EHands** particularly useful for non-stationary signal analysis and noise/interference reduction directly on quantum hardware. A carefully chosen polynomial can adapt to varying signal characteristics, enhancing accuracy in dynamic environments.

The ability to perform batch processing using vectorized quantum operations makes the **EHands protocol** a valuable tool for tasks such as computing batch-average mean square error (MSE) on a QPU in ML-regression problems. Notably, the MSE, when measured as the expectation value of a single qubit, serves as a local cost function, helping to mitigate the problem of barren plateaus. The details of the MSE implementation are discussed in [Section B](#).

In quantum image processing (QImP) [25–27] polynomial-based filters play a crucial role in edge detection and noise reduction. By integrating the **EHands protocol** with efficient image encoding strategies, such as **QCrank**, these image processing tasks can be performed solely on the quantum device. This integration could drive significant advancements in quantum-enhanced image analysis pipelines.

Note that the performance of the **EHands** algorithm is currently evaluated using the **EVEN** encoding. However, future quantum sensors are expected to interface directly with QPUs while preserving quantum information [28–30], thereby eliminating the need to encode classical input data through the **EVEN** scheme. Such direct

integration would significantly enhance the practical applicability of the **EHands** algorithm.

Despite its flexibility and efficiency, the **EHands protocol** faces scalability challenges when measuring expectation values for higher-degree polynomials. Due to signal attenuation of $\mathcal{O}(1/d)$, achieving accurate results requires increasing the number of measurements, which scale as $\mathcal{O}(d^2)$ to maintain the precision. While increasing shot counts can partially address this issue, exploring amplitude amplification techniques may provide more efficient solutions.

In conclusion, **EHands** represents a significant step forward in leveraging quantum hardware for real-world applications that rely on polynomial computations. Its potential spans multiple domains, including QML, signal processing, and image analysis, where efficient polynomial transformations are essential. As quantum hardware continues to advance, the scalability and adaptability of the **EHands protocol** make it a promising candidate for further development and integration into more complex quantum computing frameworks.

For the sake of reproducibility and transparency, all circuits and experimental results used in this paper are publicly available in the repository <https://github.com/QuantumComputingLab/qpixlpp/> in the `examples` folder.

ACKNOWLEDGMENTS

This research was supported by the U.S. Department of Energy (DOE) under Contract No. DE-AC02-05CH11231, through the Office of Science, Office of Advanced Scientific Computing Research (ASCR) Exploratory Research for Extreme-Scale Science and Accelerated Research in Quantum Computing. This research used resources of two DOE user facilities: the National Energy Research Scientific Computing Center (NERSC) located at Lawrence Berkeley National Laboratory, operated under Contract No. DE-AC02-05CH11231, and the Oak Ridge Leadership Computing Facility, operated under Contract No. DE-AC05-00OR22725.

-
- [1] P. W. Shor, Algorithms for quantum computation: discrete logarithms and factoring, in *Proceedings 35th Annual Symposium on Foundations of Computer Science* (1994) pp. 124–134.
 - [2] L. K. Grover, A fast quantum mechanical algorithm for database search, in *Proceedings of the 28th Annual ACM Symposium on Theory of Computing* (1996) pp. 212–219.
 - [3] A. W. Harrow, A. Hassidim, and S. Lloyd, Quantum algorithm for linear systems of equations, *Phys. Rev. Lett.* **103**, 150502 (2009).
 - [4] G. H. Low and I. L. Chuang, Optimal Hamiltonian simulation by quantum signal processing, *Phys. Rev. Lett.* **118**, 010501 (2017).
 - [5] V. Vedral, A. Barenco, and A. Ekert, Quantum networks for elementary arithmetic operations, *Phys. Rev. A* **54**, 147 (1996).
 - [6] Y. Takahashi and N. Kunihiro, A linear-size quantum circuit for addition with no ancillary qubits, *Quantum Inf. Comput.* **5**, 440 (2005).
 - [7] Y. Takahashi and N. Kunihiro, A fast quantum circuit for addition with few qubits, *Quantum Inf. Comput.* **8**, 636 (2008).

- [8] Y. Takahashi, Quantum arithmetic circuits: A survey, *IEICE Trans. Fundam. Electron. Commun. Comput. Sci.* **E92.A**, 1276 (2009).
- [9] S. Wang, X. Li, W. J. B. Lee, S. Deb, E. Lim, and A. Chattopadhyay, A comprehensive study of quantum arithmetic circuits, *Philos. Trans. R. Soc. A* **383**, 20230392 (2025).
- [10] G. H. Low and I. L. Chuang, Optimal Hamiltonian simulation by quantum signal processing, *Phys. Rev. Lett.* **118**, 010501 (2017).
- [11] Y. Dong, L. Lin, H. Ni, and J. Wang, Infinite quantum signal processing, *Quantum* **8**, 1558 (2024).
- [12] A. Gilyén, Y. Su, G. H. Low, and N. Wiebe, Quantum singular value transformation and beyond: exponential improvements for quantum matrix arithmetics, in *Proceedings of the 51st Annual ACM SIGACT Symposium on Theory of Computing* (2019) pp. 193–204.
- [13] Y. Dong, L. Lin, and Y. Tong, Ground-state preparation and energy estimation on early fault-tolerant quantum computers via quantum eigenvalue transformation of unitary matrices, *PRX Quantum* **3**, 40305 (2022).
- [14] M. Kessler, D. Alonso, and P. Sánchez, Determination of the number of shots for grover’s search algorithm, *EPJ Quantum Technol.* **10**, 47 (2023).
- [15] L.-Z. Liu and at al, Full-period quantum phase estimation, *Phys. Rev. Lett.* **130**, 120802 (2023).
- [16] Z. He, D. Amaro, R. Shaydulin, and M. Pistoia, Performance of quantum approximate optimization with quantum error detection, *Commun. Phys.* **8**, 217 (2025).
- [17] S. Herbert, Quantum monte carlo integration: The full advantage in minimal circuit depth, *Quantum* **6**, 823 (2022).
- [18] R. A. Abrahao, A. Mansouri, and A. P. Lund, Boson sampling with gaussian input states: Toward efficient scaling and certification, *Phys. Rev. A* **110**, 052437 (2024).
- [19] E. Recio-Armengol and J. Bowles, IQPopt: Fast optimization of instantaneous quantum polynomial circuits in JAX, arXiv: [10.48550/arXiv.2501.04776](https://arxiv.org/abs/10.48550/arXiv.2501.04776) (2025).
- [20] M. Rath and H. Date, Quantum data encoding: a comparative analysis of classical-to-quantum mapping techniques and their impact on machine learning accuracy, *EPJ Quantum Technol.* **11**, 72 (2024).
- [21] J. J. Wallman and J. Emerson, Noise tailoring for scalable quantum computation via randomized compiling, *Phys. Rev. A* **94**, 052325 (2016).
- [22] P. D. Nation and M. Treinish, Suppressing quantum circuit errors due to system variability, *PRX Quantum* **4**, 010327 (2023).
- [23] M. G. Amankwah, D. Camps, E. W. Bethel, R. Van Beeumen, and T. Perciano, Quantum pixel representations and compression for N-dimensional images, *Sci. Rep.* **12**, 7712 (2022).
- [24] J. Balewski, M. G. Amankwah, R. Van Beeumen, E. W. Bethel, T. Perciano, and D. Camps, Quantum-parallel vectorized data encodings and computations on trapped-ion and transmon QPUs, *Sci. Rep.* **14**, 3435 (2024).
- [25] S. E. Venegas-Andraca and S. Bose, Storing, processing, and retrieving an image using quantum mechanics, in *Quantum Information and Computation*, Vol. 5105, edited by E. Donkor, A. R. Pirich, and H. E. Brandt, International Society for Optics and Photonics (SPIE, 2003) pp. 137–147.
- [26] F. Yan and S. E. Venegas-Andraca, Lessons from twenty years of quantum image processing, *ACM Transactions on Quantum Computing* **6**, 1 (2025).
- [27] L. Wei, H. Liu, J. Xu, L. Shi, Z. Shan, B. Zhao, and Y. Gao, Quantum machine learning in medical image analysis: A survey, *Neurocomputing* **525**, 42 (2023).
- [28] D. Awschalom and at al, Development of quantum interconnects (QuICs) for next-generation information technologies, *PRX Quantum* **2**, 017002 (2021).
- [29] Y. Sekiguchi, Y. Yasui, K. Tsurumoto, *et al.*, Geometric entanglement of a photon and spin qubits in diamond, *Commun. Phys.* **4**, 264 (2021).
- [30] Z. Chen, Transferring four-dimensional atomic states at one step between separated cavities, *J. Phys. Conf. Ser.* **2595**, 012002 (2023).
- [31] B. Evert, Z. G. Izquierdo, J. Sud, H.-Y. Hu, S. Grabbe, E. G. Rieffel, M. J. Reagor, and Z. Wang, Syncopated dynamical decoupling to suppress crosstalk in quantum circuits, *Phys. Rev. Appl.* , (2025).

APPENDIXES

In the Appendixes, we discuss in detail the derivation of the **EHands protocol** presented in the main text. In [Section A](#), we describe the **EVEN** encoding and decoding schemes together with the four key **EHands** quantum circuits implementing *multiplication*, *addition*, *negation*, and *parity flip*. We further generalize the weighted sum circuit to compute the linear combination of three real numbers and extend the **EHands protocol** to multivariable polynomials. [Section B](#) discusses the computation of the mean squared error (MSE) as a specific example. [Section C](#) presents numerical simulations that complement the experimental results reported in the main text, while [Section D](#) details additional exploratory experiments on IBM hardware that motivates our choice of error mitigation techniques. Finally, [Section E](#) introduces an alternative implementation of $P_d(x)$ with CNOT depth scaling as $\mathcal{O}(\log d)$.

Appendix A: State vectors and observables for EHands protocol

1. EVEN encoding and decoding of 2 real numbers on 2 qubits

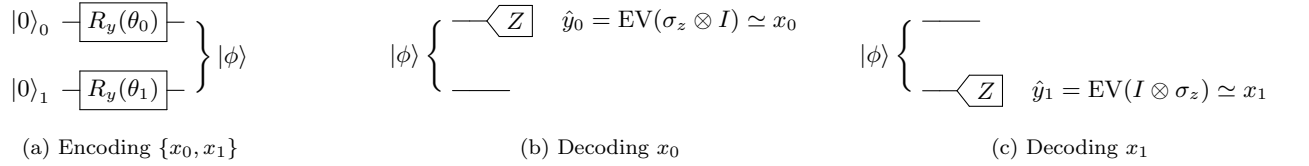
Encoding. Let us consider 2 real values $\{x_0, x_1\}$ in the range $[-1, 1]$. The encoding process involves mapping each value x_i to an angle θ_i :

$$\theta_i = \arccos(x_i), \quad i = 0, 1. \quad (\text{A1})$$

These angles parameterize rotation gates $R_y(\theta_i)$, which are then applied to a 2-qubit quantum state initialized in $|00\rangle$:

$$|\phi\rangle = [R_y(\theta_0) \otimes R_y(\theta_1)] |00\rangle = \begin{bmatrix} \cos(\theta_0/2) \cos(\theta_1/2) \\ \cos(\theta_0/2) \sin(\theta_1/2) \\ \sin(\theta_0/2) \cos(\theta_1/2) \\ \sin(\theta_0/2) \sin(\theta_1/2) \end{bmatrix} = \frac{1}{2} \begin{bmatrix} \sqrt{1+x_0}\sqrt{1+x_1} \\ \sqrt{1+x_0}\sqrt{1-x_1} \\ \sqrt{1-x_0}\sqrt{1+x_1} \\ \sqrt{1-x_0}\sqrt{1-x_1} \end{bmatrix}, \quad (\text{A2})$$

where we applied the last equality Eq. (A1) and relationships between trigonometric and inverse trigonometric functions. The resulting state $|\phi\rangle$, shown also as [Circuit 1a](#), *encodes* the classical information about $\{x_0, x_1\}$.



CIRCUIT 1: (a) Encoding of 2 real numbers $\{x_0, x_1\}$ in a 2-qubit state $|\phi\rangle$. (b)–(c) Decoding is performed by measuring the expectation value of the Pauli-Z operator on the corresponding qubit.

Decoding. In order to retrieve either of the value $\{x_0, x_1\}$ encoded in the state $|\phi\rangle$, we define two complementary operators

$$O_s := \sigma_z \otimes I = \begin{bmatrix} 1 & 0 & 0 & 0 \\ 0 & 1 & 0 & 0 \\ 0 & 0 & -1 & 0 \\ 0 & 0 & 0 & -1 \end{bmatrix}, \quad O_p := I \otimes \sigma_z = \begin{bmatrix} 1 & 0 & 0 & 0 \\ 0 & -1 & 0 & 0 \\ 0 & 0 & 1 & 0 \\ 0 & 0 & 0 & -1 \end{bmatrix}, \quad (\text{A3})$$

which represent measurements of qubit q_0 or qubit q_1 in the Z -basis, respectively. We measure expectation values (EV) of the operators O_s, O_p , yielding back the estimators of the input values

$$\langle \phi | O_s | \phi \rangle = \hat{x}_0, \quad \langle \phi | O_p | \phi \rangle = \hat{x}_1. \quad (\text{A4})$$

The *decoding* quantum circuits are depicted in [Circuits 1b](#) and [1c](#), where $\langle Z \rangle$ denotes measuring the EV of the corresponding qubit in the Z -basis.

2. Product-with-memory circuit

After establishing a method to encode and decode a pair of real values using a 2-qubit system, we introduce a unitary U_{prod} to compute their product. When U_{prod} is applied to the state $|\phi\rangle$, as defined in Eq. (A2), it produces a new state $|\psi_{\Pi}\rangle$. The expectation value (EV) of O_p for this state corresponds to the estimator of the product $x_0 x_1$.

Let $R_z(\pi/2) = e^{-i\frac{\pi}{4}} \begin{bmatrix} 1 & 0 \\ 0 & i \end{bmatrix}$. We define the *product*-unitary U_{prod} as follows

$$U_{\text{prod}} := \text{CNOT}_{0,1} \cdot [I \otimes R_z(\pi/2)] = e^{-i\frac{\pi}{4}} \begin{bmatrix} 1 & 0 & 0 & 0 \\ 0 & i & 0 & 0 \\ 0 & 0 & 0 & i \\ 0 & 0 & 1 & 0 \end{bmatrix}. \quad (\text{A5})$$

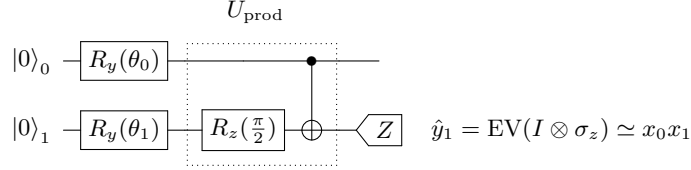
Next, by applying U_{prod} to the encoded state $|\phi\rangle$ given in Eq. (A2), we obtain the state

$$|\psi_{\Pi}\rangle = U_{\text{prod}} |\phi\rangle = \frac{e^{-i\frac{\pi}{4}}}{2} \begin{bmatrix} \sqrt{1+x_0}\sqrt{1+x_1} \\ i\sqrt{1+x_0}\sqrt{1-x_1} \\ i\sqrt{1-x_0}\sqrt{1-x_1} \\ \sqrt{1-x_0}\sqrt{1+x_1} \end{bmatrix}, \quad (\text{A6})$$

so that the EV of O_p returns the product of the 2 inputs

$$\langle\psi_{\Pi}|O_p|\psi_{\Pi}\rangle = x_0x_1. \quad (\text{A7})$$

The corresponding quantum [Circuit 2](#) performs $\hat{y}_1 = x_0x_1$. It includes the initial state preparation, where the rotation angles θ_i are computed as in Eq. (A1).



CIRCUIT 2: Computing product x_0x_1 as the expectation value of σ_z operator measured on q_1 .

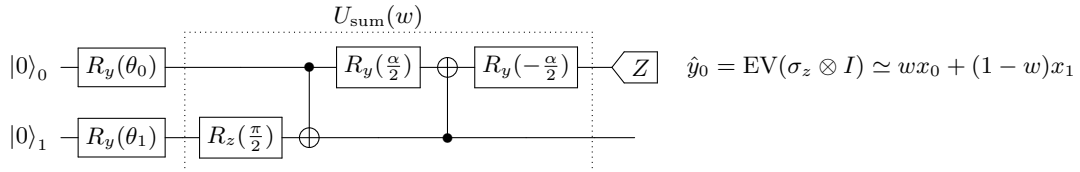
Note that U_{prod} does not affect qubit q_0 . As a result, this qubit retains the information about its input value x_0 . Hence, the EV of O_s after applying U_{prod} remains unchanged

$$\langle\psi_{\Pi}|O_s|\psi_{\Pi}\rangle = x_0. \quad (\text{A8})$$

For a general input vector of length N , the EVEN encoding requires N qubits for data storage. The product-with-memory operation scales linearly with the number of input pairs, requiring $\mathcal{O}(N)$ CNOT gates with a circuit depth of $\mathcal{O}(1)$ for parallel multiplication operations, or $\mathcal{O}(N)$ for sequential operations depending on the specific implementation and connectivity constraints of the target quantum processor.

3. Weighted sum circuit

Our next goal is to compute linear combinations of a pair of real numbers. These numbers are again encoded in the 2-qubit state $|\phi\rangle$, as defined in Eq. (A2). To do so, we introduce the unitary U_{sum} . When U_{sum} is applied to the state $|\phi\rangle$, it produces a new state $|\psi_{\Sigma}\rangle$. The expectation value (EV) of O_s for this state corresponds to the estimator of the weighted sum $wx_0 + (1-w)x_1$, where the relative weight $w \in [0, 1]$. [Circuit 3](#) encapsulates this entire process.



CIRCUIT 3: Computing weighted sum $wx_0 + (1-w)x_1$ as EV of σ_z operator measured on q_0 .

The unitary U_{sum} contains a rotation parameter α which depends on w as follows

$$\alpha = \arccos(1 - 2w). \quad (\text{A9})$$

To prove the above, we start by expressing the rotation matrices $R_y(\alpha/2)$ and $R_y(-\alpha/2)$, with $\alpha \in [0, \pi]$, in terms of the parameter w :

$$R_y(\pm \alpha/2) = \frac{1}{\sqrt{2}} \begin{bmatrix} \sqrt{1+\sqrt{1-w}} & \mp \sqrt{1-\sqrt{1-w}} \\ \pm \sqrt{1-\sqrt{1-w}} & \sqrt{1+\sqrt{1-w}} \end{bmatrix}, \quad (\text{A10})$$

and define the parameterized *sum*-unitary $U_{\text{sum}}(w)$ as follows

$$U_{\text{sum}}(w) := [R_y(-\alpha/2) \otimes I] \cdot \text{CNOT}_{1,0} \cdot [R_y(\alpha/2) \otimes I] \cdot U_{\text{prod}} = e^{-i\frac{\pi}{4}} \begin{bmatrix} 1 & 0 & 0 & 0 \\ 0 & i\sqrt{w} & \sqrt{1-w} & 0 \\ 0 & 0 & 0 & i \\ 0 & i\sqrt{1-w} & -\sqrt{w} & 0 \end{bmatrix}. \quad (\text{A11})$$

Next, by applying $U_{\text{sum}}(w)$ to the encoded state $|\phi\rangle$ given in Eq. (A2), we obtain the state

$$|\psi_{\Sigma}\rangle = U_{\text{sum}}(w) |\phi\rangle = \frac{e^{-i\frac{\pi}{4}}}{2} \begin{bmatrix} \sqrt{1+x_0}\sqrt{1+x_1} \\ i\sqrt{w}\sqrt{1+x_0}\sqrt{1-x_1} + \sqrt{1-w}\sqrt{1-x_0}\sqrt{1+x_1} \\ i\sqrt{1-x_0}\sqrt{1-x_1} \\ i\sqrt{1-w}\sqrt{1+x_0}\sqrt{1-x_1} - \sqrt{w}\sqrt{1-x_0}\sqrt{1+x_1} \end{bmatrix}, \quad (\text{A12})$$

so that the EV of O_s returns the weighted sum of the 2 inputs

$$\langle\psi_{\Sigma}|O_s|\psi_{\Sigma}\rangle = wx_0 + (1-w)x_1. \quad (\text{A13})$$

Note that the first 2 gates of U_{sum} are equal to U_{prod} and the remaining gates of U_{sum} do not change q_1 in Circuit 3, hence, qubit q_1 contains the x_0x_1 product, i.e.,

$$\langle\psi_{\Sigma}|O_p|\psi_{\Sigma}\rangle = x_0x_1. \quad (\text{A14})$$

For the special choice of $w = 1/2 \rightarrow \alpha = \pi/2$ the result of Eq. (A13) is a plain average: $(x_0 + x_1)/2$.

For completeness, Table III lists other possible algebraic operations on x_0 and x_1 enabled by Circuit 3. These operations are obtained by measuring the qubits of the final state $|\psi_{\Sigma}\rangle$ in other bases.

TABLE III. Expectation values for Circuit 3 for projective single-qubit measurement in the X , Y , and Z bases.

Measurement Basis	EV[q_0] = $\langle\psi_{\Sigma} O_p \psi_{\Sigma}\rangle$	EV[q_1] = $\langle\psi_{\Sigma} O_p \psi_{\Sigma}\rangle$
$\text{---}\langle X \rangle^{\text{a}}$	$\sqrt{w(1-w)}(x_0 - x_1)$	$\sqrt{1-w} \cdot \sqrt{1-x_0^2}$
$\text{---}\langle Y \rangle^{\text{b}}$	$\sqrt{1-x_0^2} \cdot \sqrt{1-x_1^2}$	$\sqrt{w} \cdot \sqrt{1-x_1^2}$
$\text{---}\langle Z \rangle$	$w \cdot x_0 + (1-w) \cdot x_1$	$x_0 \cdot x_1$

^a Measuring in the X -basis: $\text{---}\langle H \rangle\langle Z \rangle$

^b Measuring in the Y -basis: $\text{---}\langle S^\dagger \rangle\langle H \rangle\langle Z \rangle$

4. Linear combinations by concatenating summation circuits

We now generalize Circuit 3 to compute the linear combination of three real numbers. This generalization uses three qubits and two different U_{sum} gates. Our objective is to compute the linear combination of 3 real values $\{x_0, x_1, x_2\} \in [-1, 1]$:

$$s_3 = a_0x_0 + a_1x_1 + a_2x_2, \quad (\text{A15})$$

where the coefficients satisfy the following constraints

$$a_0 + a_1 + a_2 = 1, \quad a_i \in [0, 1]. \quad (\text{A16})$$

Strictly speaking, the coefficients a_i must be non-negative. However, we will later introduce a trick involving the insertion of X -gates, enabling us to also handle cases with negative coefficients as well.

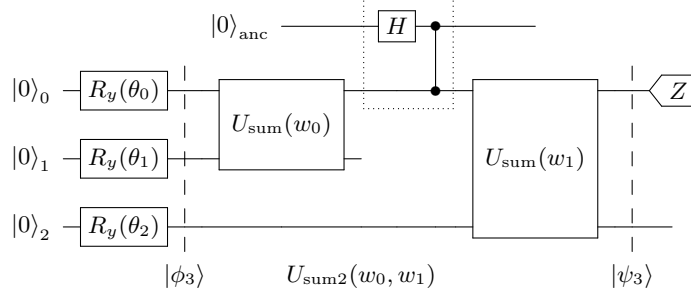
First, we need to expand the input EVEN encoding to encode 3 real values in the following 3-qubit state

$$|\phi_3\rangle = [R_y(\theta_0) \otimes R_y(\theta_1) \otimes R_y(\theta_2)] |000\rangle, \quad (\text{A17})$$

where θ_i are given in Eq. (A1). Intuitively, the concatenation of two U_{sum} circuits is expect to produce

$$s_3 = w_1 [w_0 x_0 + (1 - w_0) x_1] + (1 - w_1) x_2 = \underbrace{w_1 w_0}_{a_0} \cdot x_0 + \underbrace{w_1 (1 - w_0)}_{a_1} \cdot x_1 + \underbrace{(1 - w_1)}_{a_2} \cdot x_2, \quad (\text{A18})$$

where the two $U_{\text{sum}2}$ -parameters w_0 and w_1 can be found by solving the set of Eqs. (A15) and (A18). The particular case of $w_0 = 1/2$, $w_1 = 2/3$ results in the plain average over 3 numbers: $(x_0 + x_1 + x_2)/3$. The corresponding quantum circuit, shown in Circuit 4, combines $U_{\text{sum}}(w_0)$, acting on qubits $\{0, 1\}$, with $U_{\text{sum}}(w_1)$, acting on qubits $\{0, 2\}$.



CIRCUIT 4: Circuit yielding expectation value being the weighted sum of 3 input values $\text{EV} = w_1 [w_0 x_0 + (1 - w_0) x_1] + (1 - w_1) x_2$.

Measuring qubit q_0 in Circuit 4 for the operator $O_{s3} := \sigma_z \otimes I \otimes I$ and state $|\psi_3\rangle = U_{\text{sum}2} |\phi_3\rangle$, yields the EV

$$\langle \psi_3 | O_{s3} | \psi_3 \rangle = w_1 [w_0 x_0 + (1 - w_0) x_1] + (1 - w_1) x_2. \quad (\text{A19})$$

The use of the parity-flip operator, indicated by the dotted rectangle in Circuit 4, is essential to obtain the correct result in Eq. (A19). Omitting this operator introduces an unwanted term in the output, specifically the additional square root term shown in Eq. (A20):

$$w_1 [w_0 x_0 + (1 - w_0) x_1] + (1 - w_1) x_2 + \frac{1}{2} \sqrt{(-1 + w_1) w_1} \sqrt{1 - x_0^2} \sqrt{1 - x_1^2} \sqrt{1 - x_2^2}. \quad (\text{A20})$$

Thus, the parity-flip operator in Circuit 4 serves to cancel the additional square roots term.

If the reversibility is not required, the *ancilla* qubit can be reset and reused after the CZ gate is applied. Similarly, qubits 1 and 2 can be reset and reused after their respective gate blocks are completed, enabling efficient qubit recycling for more complex **EHands** circuits.

Note that it is possible to obtain a modified version of Circuit 4 to handle a sum with a negative coefficient $a_j < 0$. This can be achieved by inserting an X -gate before the $R_y(\theta_j)$ gate for the specific input qubit q_j . It is equivalent to flipping the sign of $x_j \rightarrow -x_j$ while using $|a_j| > 0$.

Circuit 4 can be further generalized to compute a weighted sum over K inputs by concatenating $K - 1$ U_{sum} unitaries, interspersed with $K - 2$ parity-flip operators consuming $K - 2$ ancillas. For any set of desired coefficients a_i , subject to

$$\sum_i a_i = 1, \quad a_i \in [0, 1], \quad (\text{A21})$$

it is always possible to determine $K - 1$ U_{sum} -parameters w_j . E.g. a plain average over K variables: $\frac{1}{K} \sum_{i=0}^{K-1} x_i$ can be obtained using weights: $w_i = \frac{i+1}{i+2}$ for $i \in [0, \dots, K - 2]$.

5. Polynomial in multiple variables

The **EHands** protocol can be extended to compute higher degree polynomials involving multiple variables. Consider a polynomial $p(x_1, x_2, \dots, x_n)$ of degree d , which can be expressed as:

$$p(x_1, x_2, \dots, x_n) = \sum_{i=0}^d a_i x_1^{i_1} x_2^{i_2} \dots x_n^{i_n}, \quad (\text{A22})$$

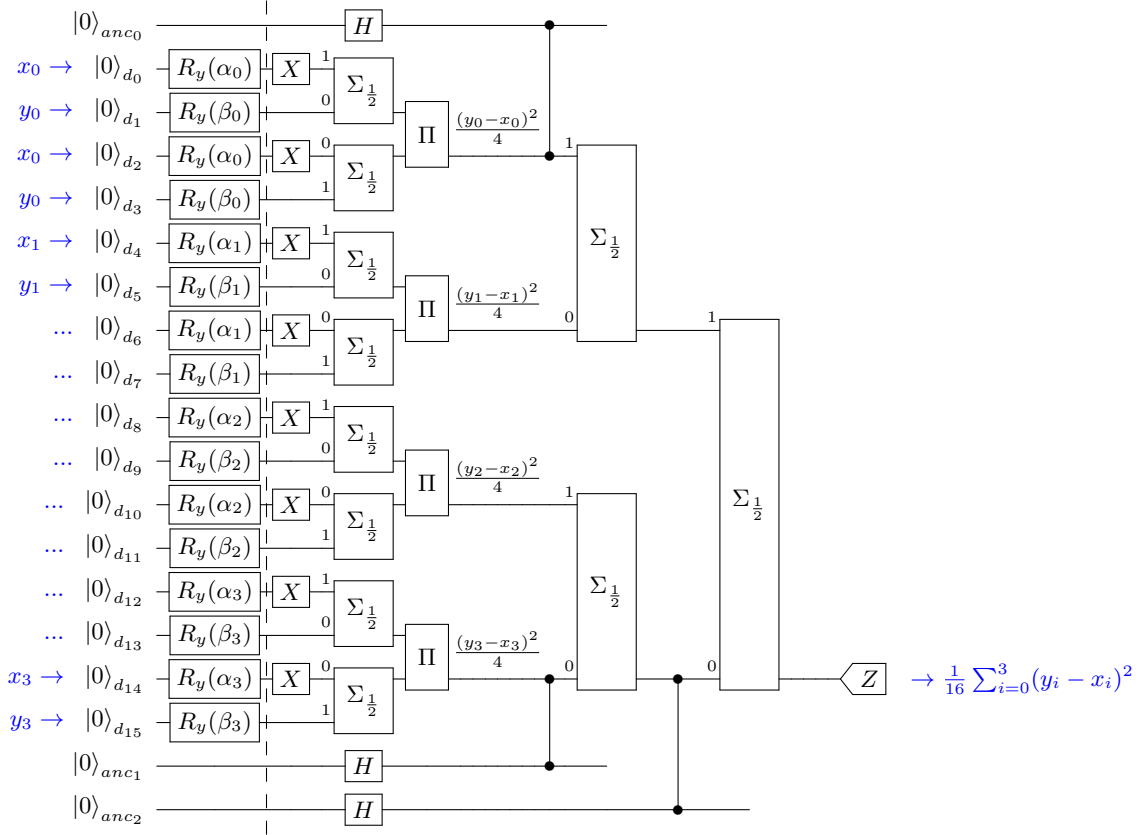
where a_i are real coefficients, and each term $x_1^{i_1} x_2^{i_2} \dots x_n^{i_n}$ represents a product of the input variables raised to different powers, with $i_1 + i_2 + \dots + i_n \leq d$. All input values x_i and coefficients a_i are constrained to the range $[-1, 1]$, ensuring that the polynomial terms are bounded and computable within the limits of the **EHands** protocol.

Appendix B: Computation of Mean Squared Error with EHands protocol

The mean squared error (MSE) is widely used in machine learning to evaluate the performance of regression models. It measures the average squared differences between the true values y_i and predicted values x_i , helping assess model accuracy and guiding optimization processes. The MSE is defined as:

$$\text{MSE}(\mathbf{x}, \mathbf{y}) = \frac{1}{N} \sum_{i=0}^{N-1} (x_i - y_i)^2, \quad (\text{B1})$$

where N is the number of predicted values.



CIRCUIT 5: EHands computation of mean squared error (MSE) on two vectors of real values x_i, y_i of length 4. The explicit implementation of unitaries $\Sigma_{\frac{1}{2}}, \Pi$ are defined in Fig. 1 in the main text.

The EHands protocol can be used to compute the MSE on a QPU as illustrated in Circuit 5 for $N = 4$, pairs of real values, x_i, y_i . For this MSE implementation, the total CNOT count is 29 and the CNOT depth is 9. The computation proceeds as follows:

- First, the EVEN encoding is used to store 4 copies of both inputs x_i, y_i on 16 qubits, labeled d_0, \dots, d_{15} . R_y rotation angles are: $\alpha_i = \arccos x_i, \beta_i = \arccos y_i$.
- The difference between each pair of values $(y_i - x_i)$ is calculated twice. We negate all y-inputs so despite we use the sum operator with weight $w = 1/2$ the results is the difference.
- The two independent copies of the differences are multiplied, yielding the terms $\frac{1}{4}(y_i - x_i)^2$.
- Finally, those squared terms are averaged, resulting with the MSE which can be measured as the expectation value of one qubit (labeled d_{14} in Circuit 5).

The four copies of each input are necessary, because the *no-cloning* theorem prohibits using same quantum state twice, what is needed to square the values of the differences. Notice that the final output is $\text{MSE}/4$ which is a characteristic

feature of the **EHands protocol**, due to how the square of the difference is computed. This attenuation factor of 4 remains unchanged as the number of input variables (N) increases. For the purpose of minimization, a constant scaling of the loss does not pose a problem. However, in practice, more shots are required to achieve a given statistical accuracy for the MSE.

In general, the quantum resources required to compute MSE for N pairs of real values x_i, y_i using the **EHands protocol** and serial sum implementation are as follows: (i) $4N + \mathcal{O}(\log N)$ qubits, (ii) $5N + \mathcal{O}(\log N)$ CNOT gates, (iii) $\mathcal{O}(\log N)$ CNOT depth, (iv) one qubit measured at the end.

The potential application of vectorized MSE computation using the **EHands protocol** with the **QCrank** encoding [24] include, for example, the computation of batch-average loss for QML applications. The edge detection for gray-scale images is another example. It is one of the simplest and most useful image-processing operations is edge detection, which involves computing the squared gradient between pairs of pixels and applying a threshold on it. The threshold can be easily adjusted to account for reduced gradient magnitudes caused by limited gate fidelity on the NISQ hardware. This approach may require more shots to achieve comparable precision on hardware versus an ideal simulator.

Appendix C: Numerical simulations

To demonstrate the flexibility of the **EHands protocol**, we selected three common functions listed in [Table IV](#). Each function was approximated by a polynomial of degree 5 or 6, depending on its parity, through classical pre-processing. These polynomials were then implemented as **EHands** quantum circuits by naturally extending the pattern shown in [Fig. 2a](#) in the main text to the required degree d .

TABLE IV. Polynomial approximations of selected functions for testing the performance of the reversible **EHands protocol** in ideal simulations.

target function	Fig. 4 panel	poly degree	num CNOT	num qubits	used shots ^a
$\exp(2x)$	a	5	23	15	2e5
$\arctan(5x)$	b	5	23	15	1e7
$\exp(-9x^2)$	c	6	28	18	8e7

^a number of shots per x -data point

Those 3 quantum circuits were simulated using the shot-based ideal Qiskit simulator for a grid of 21 equally spaced input values $x \in [-1, 1]$. As shown in [Fig. 4](#), the simulated Qiskit results closely match the analytical values of each polynomial (solid line), demonstrating strong agreement and confirming the accuracy of our approach.

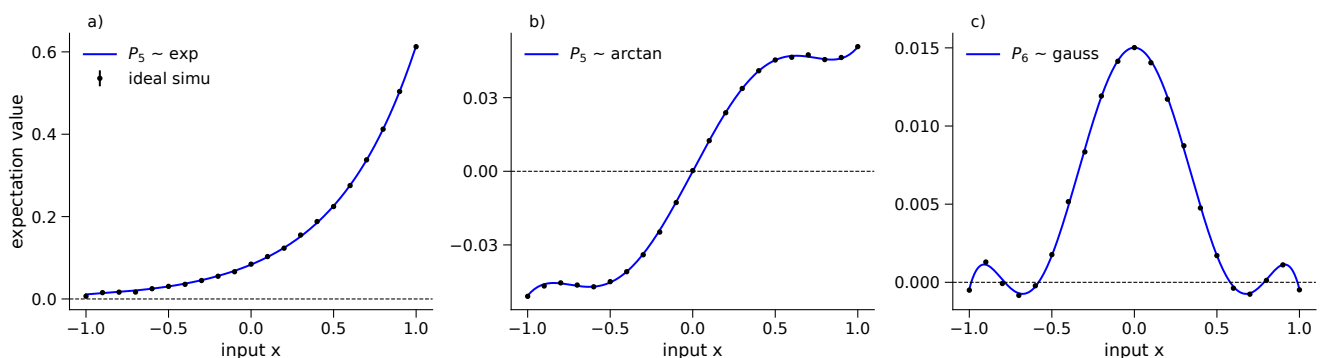


FIG. 4. Polynomial approximations of the selected functions listed in [Table IV](#) are accurately reproduced by ideal Qiskit simulations. The solid curves represent the ground truth, while the data points, shown with statistical error bars, were obtained from a shot-based simulator using the number of shots specified in the last column of the table.

Appendix D: Hardware performance optimization

The results of executing `EHands` protocol on IBM hardware, shown in Fig. 3 in the main text, represent the best performance observed on the day the experiments were conducted (May 2025). For those main results, we employed randomized compilation and optimized qubit mapping; however, we did not utilize dynamic decoupling or zero noise extrapolation. In this section, we present additional exploratory experiments on the IBM hardware that justify our choices of error mitigation tools.

1. Impact of randomized compilation and dynamic decoupling

Randomized compilation (RC), also known as Pauli twirling, mitigates coherent errors by converting them into stochastic noise. Dynamic decoupling (DD) inserts a carefully timed sequence of pulses to each qubit timeline, aiming to cancel a portion of the surrounding noise. Potentially, combining these techniques yields more reliable and statistically robust results on NISQ devices [31].

For one particular choice of $P_d(x) \sim \arctan(x)$ polynomial and using one of the best-performing QPU on the day the research was conducted—namely IBM Marrakesh—we examined the impact of enabling RC, DD, and qubit mappings on the fidelity of the outcome. This was done for three *a priori* equivalent qubit layouts, each selected by the standard IBM transpiler using different random seeds. All 12 jobs were executed within 2 hours wall-time. The MSE between ground truth polynomial value and the measurement was the infidelity metric of choice. The results are shown in Table V and in Fig. 5.

TABLE V. MSE for $P_d(x) \sim \arctan(x)$ polynomial transpiled to different subset of qubits and executed on IBM Marrakesh with and without randomized compilation. MSE was multiplied by $1e4$ for clarity.

mapping	qubits	MSE raw	MSE only RC	MSE w/ RC+DD	MSE only DD
map1	44, 42, 56, 43, 45, 46, 47, 37, 57	1.1 ± 0.3	0.4 ± 0.1	1.1 ± 0.3	2.4 ± 0.7
map2	9, 27, 28, 17, 7, 5, 6, 8, 4	7.1 ± 2.2	4.4 ± 1.4	4.1 ± 1.3	15.6 ± 4.8
map3	107, 109, 87, 97, 106, 105, 104, 108, 117	10.8 ± 3.3	1.7 ± 0.5	1.1 ± 0.3	3.5 ± 1.1

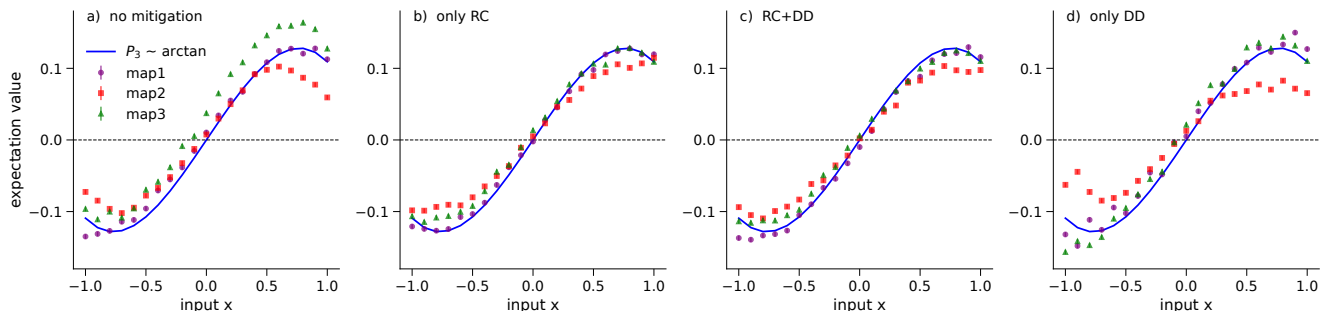


FIG. 5. Impact of randomized compilation (RC) and/or dynamic decoupling (DD) on MSE of $P_3(x) \sim \arctan(x)$ measured on IBM Marrakesh for the same circuit transpiled onto three sets of qubits, labeled as map1, 2, 3. See Table V for the details, including MSE of each measurement.

Due to the daily variability in the calibration of the Marrakesh QPU, the specific choice of qubits lacks intrinsic significance. We list the three sets of 9 qubit mappings here for illustrative purposes only. Randomized compilation and dynamical decoupling were enabled individually and in combination using the `Qiskit SamplerOptions()`. For RC, we selected twirling for both gates and measurements, setting the number of randomizations to 60. For DD, we used the 'XX' sequence type, with slack distribution set to 'middle' and scheduling configured as 'ALAP'. To keep statistical error constant we always used the same total number of shots per circuit.

The improvement due to enabled randomized compilation was significant, as was the manual selection of the optimal qubit mapping, as shown in Fig. 5b. In contrast, the effect of dynamical decoupling (DD) was only marginal, resulting in a change in mean squared error (MSE) within one standard deviation (see panel c and d). Therefore, applying Occam's razor principle, we decided to omit DD. While it is possible to combine RC with the zero noise extrapolation

(ZNE) technique for enhanced noise mitigation, doing so would require submitting several times more jobs and is beyond the scope (and budget) of this paper.

Based on this study, we have concluded that all IBM hardware results in this work will be executed using both RC and optimal qubit mapping selection, while omitting DD and ZNE.

2. Selection of qubit mapping on hardware

To confirm and better justify our decision to manually select the optimal qubit mapping, using the Qiskit command `transpile(qc, backend, optimization_level=3, random_seed=42)`, we conducted all experiments presented in the main paper twice, using two different mappings, and chose the one with the observed smaller mean squared error (MSE). We enabling randomized compilation for all those experiments, as discussed in the previous section. This section provides all results and discussion of the procedure we employed.

For the given input circuit, the `EHands` circuits require only a small subset of the qubits available on IBM QPUs. The Qiskit transpiler automatically selects a locally optimal qubit mapping based on the current calibration of the target QPU. While the transpiler’s heuristic generally yields a good layout, it does not guarantee that a global optimum is found. By varying the transpiler’s random seed, we explored different locally optimal mappings. The only practical way to assess the quality of those different mappings is to execute the circuit on each and compare the resulting MSE to select the best mapping.

We evaluated two mappings for each of the three polynomial types across all three QPUs used in this work. Table VI lists the MSE values for all 18 tested configurations. Randomized compilation was always enabled. Figs. 6–8 present the complete set of obtained results, grouped by polynomial type. We show the better-performing mapping (i.e., the one with lower MSE) for each function–QPU pair, highlighted in red. The better results are shown in Fig. 3 in the main text.

TABLE VI. MSE dependence on the choice of 3 QPUs and 2 subsets of qubits used to execute the circuit with enabled randomized compilation. MSE was multiplied by $1e4$ for clarity.

QPU	phys qubits ^{a b}	$P_3 \sim \text{ReLU}$	$P_3 \sim \text{arctan}$	$P_2 \sim x^2$
Aachen	mapping 1	2.2 ± 0.7	0.3 ± 0.1	0.9 ± 0.3
	mapping 2	4.7 ± 1.4	3.5 ± 1.1	2.3 ± 0.7
Kingston	mapping 1	4.8 ± 1.5	0.8 ± 0.2	3.4 ± 1.0
	mapping 2	5.1 ± 1.6	1.6 ± 0.5	6.1 ± 1.9
Marrakesh	mapping 1	7.9 ± 2.4	0.5 ± 0.1	2.8 ± 0.9
	mapping 2	8.4 ± 2.6	3.0 ± 0.9	3.5 ± 1.1
shots		$2e4$	$9e4$	$9e4$

^a Mappings are different for every QPU and every polynomial

^b Mappings are ordered from the best MSE to the worst

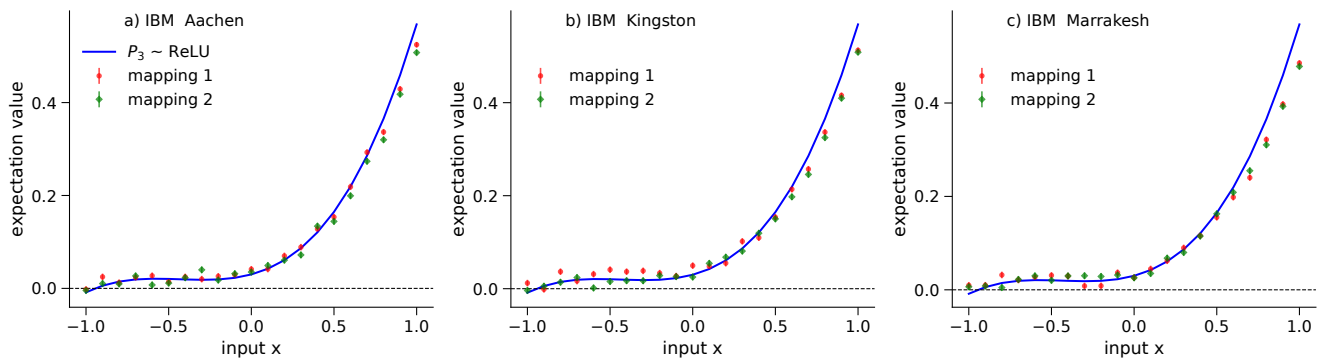


FIG. 6. Dependence of $P_3(x) \sim \text{ReLU}$ MSE fidelity on the choice of QPU and qubit subset. The randomized compilation was always enabled.

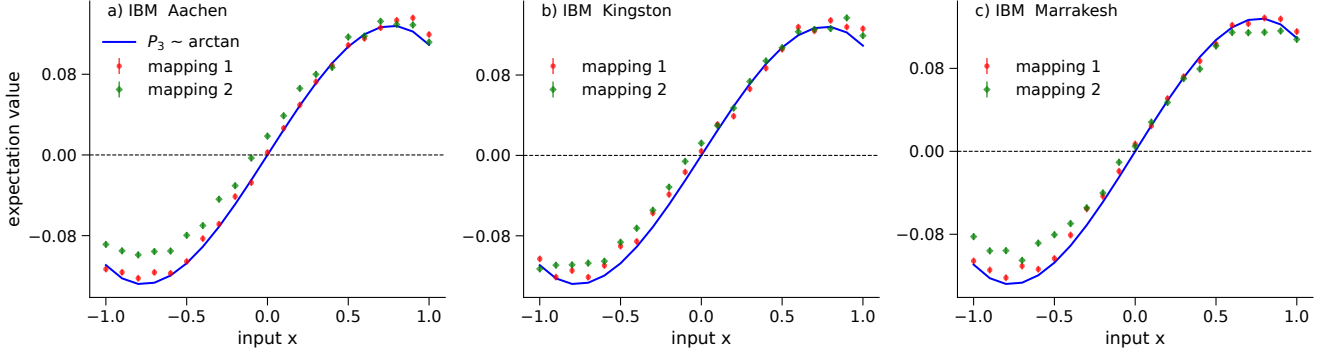


FIG. 7. Dependence of $P_3(x) \sim \arctan(x)$ MSE fidelity on the choice of QPU and qubit subset.

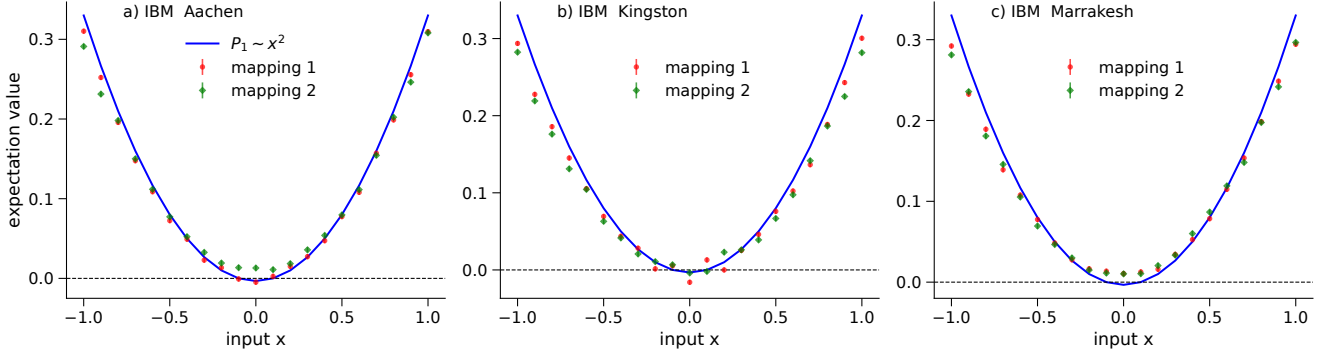


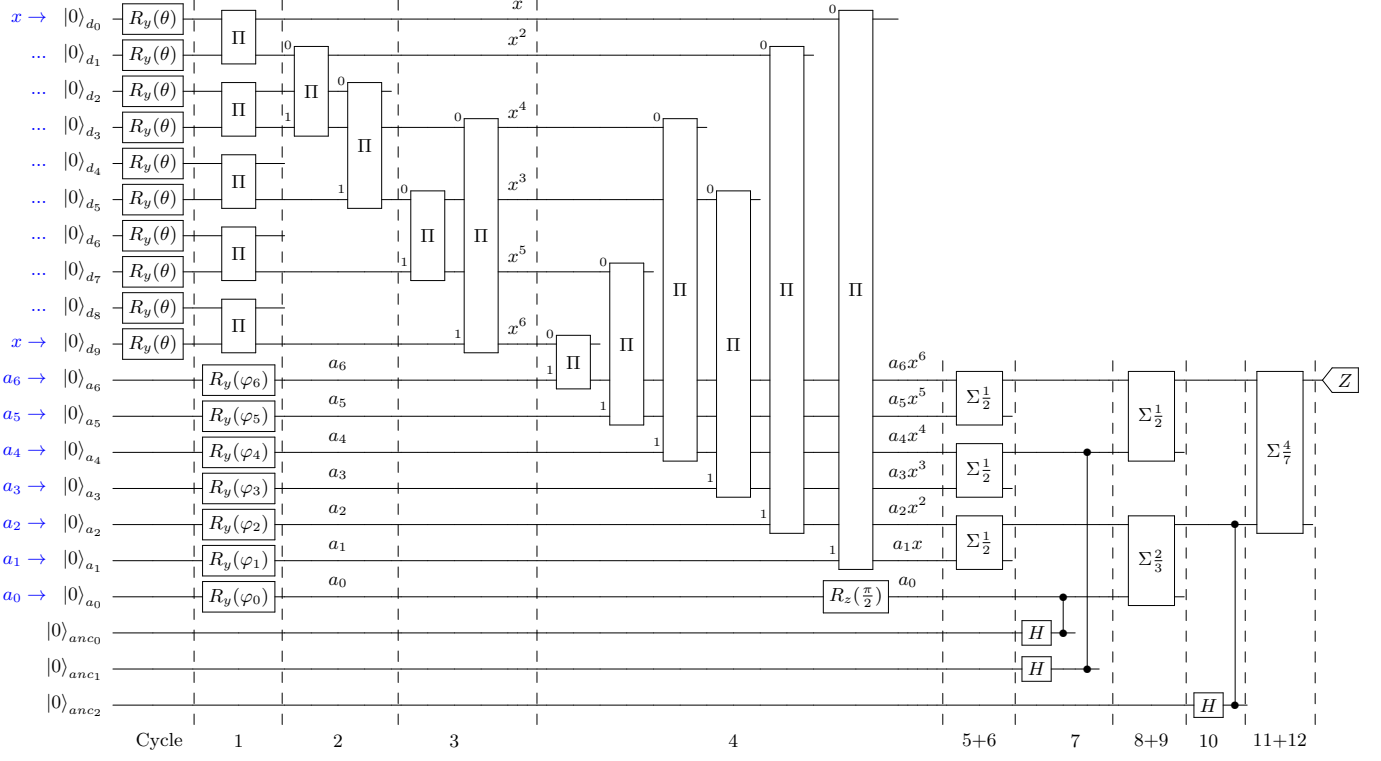
FIG. 8. Dependence of $P_2(x) \sim x^2$ MSE fidelity on the choice of QPU and qubit subset.

Appendix E: Shallow depth EHands polynomial

The main text shows two alternative implementations of $P_d(x)$. Figure 2a shows a reversible version requiring $3d$ qubits, and a non-reversible version requiring d qubits, shown in Fig. 2b. The circuits for both of these versions have the same CNOT depth of $5d - 2$.

Circuit 6 shows yet another $P_d(x)$ implementation whose CNOT gate depth scales as $\mathcal{O}(\log d)$, at the expense of storing the input in more qubits in comparison to other versions. From its construction, it is clear that $\log(d)$ depth of multiplicity operators, Π , is required to form all powers of x , up to x^d . Similarly, $\log(d)$ depth of sum operators, Σ , is required to add $d + 1$ terms for $P_d(x)$. Since it takes 1 CNOT for every Π and 2 CNOTs for every Σ , the total CNOT depth of $P_d(x)$ is of $\mathcal{O}(\log(d))$.

Naturally, one needs to compensate for the shallow circuit with more qubits carrying more copies of the input value x , to allow for the quick build-up of all powers of x without reusing the same qubits, to not violate non cloning theorem.



CIRCUIT 6: Low-depth, highly-parallel circuit for computing the polynomial $P_6(x) = \frac{1}{7}(a_6x^6 + a_5x^5 + a_4x^4 + a_3x^3 + a_2x^2 + a_1x + a_0)$.